2-D Solution for Drying with Internal Vaporization of Anisotropic Media

Patrick Perré
ENGREF/INRA, Equipe Produits Forestiers, F-54042 Nancy Cedex, France

Ian W. Turner
School of Mathematical Sciences, Queensland University of Technology, Brisbane, Q4001, Australia

Joëlle Passard
Dépt. Génie Civil, Université Henri Poincaré, NANCY 1, 54 601 Villers-les-Nancy Cedex, France

A set of physical assumptions for a straightforward and efficient simulation of the drying of a porous medium submitted to a convective and/or radiative heating is proposed. All of the parameters used are physical (liquid migration coefficient, permeability values along the thickness and the length, thermal conductivity, and external exchanges), but the relevant geometrical properties (length and thickness of the slab) were also included in the analysis. The 2-D pressure field generated within the medium during the drying process is obtained by using an analytical expression. The treatment of the pressure field, especially for a strongly anisotropic medium, is an important feature of the model, which allows an analytical model for such a complicated porous medium as wood to be used across a wide range of drying conditions. The computer code developed from the proposed formulation permits a complete simulation of the drying process within a few seconds on a personal computer. Different configurations have been tested for both anisotropic (wood) and isotropic (light concrete) porous media. Agreement with the experimental results is reasonable in terms of the observed physical phenomena. For instance, the model highlights dependence of the duration of the first drying rate on both material properties and drying conditions. This new model can be used for a global physical characterization of products by curve fitting and the collated information for the design of dryers.

Introduction

Heat and mass transfer that occurs during drying with internal vaporization can involve quite complex physical mechanisms that are strongly coupled and highly nonlinear. Consequently, in the past, numerical computation has been the preferred option for solving comprehensive sets of equations. Such models exist and have been widely documented in the literature, including work by the authors of this article (Turner and Perré, 1995; Perré and Turner, 1996). Nevertheless, because of their complexity, drying practitioners find such models cumbersome and difficult to use. In particular, these models must be supplied with numerous physical properties that are often functions of one or two variables (temperature, moisture content). Even more problematic, some of these parameters are both sensitive and poorly known. A well-documented example is relative permeability expressions. For all these reasons, this approach generally remains in laboratories, far from industrial applications.

At the other end of drying research—for example R&D, the design of dryers, and the improvement of the drying process—it is clear that the majority of the work is still closely related with empirical knowledge. Here, there is no real evidence of the use of comprehensive models, and typically experiments, curve fitting, and global formulation expressed at the scale of a whole dryer are the most popular research tools. Regarding this situation, scientists must agree that drying is often a very complex process for which the complete model-

Correspondence concerning this article should be addressed to P. Perré.

ing strategy can, in some circumstances, still fail, especially when the quality of the dried product is considered. In fact, even if it is possible to find new software devoted to the applied field of drying, the physical formulation available in these models still remains simple. This fact is evident from the dimensionless drying curves proposed by Van Meel (1958) 40 years ago (Marinos-Kouris et al., 1996), up to the pure diffusion models published recently by Pakowski and Zylla (1996). Indeed, such tools focus the attention on the global process variable, which includes matter, moisture and energy fluxes, temperature and relative humidity variations within the kiln, and so on.

The main motivation of this work is to help build a bridge between this simple modeling approach and a more comprehensive and rigorous modeling strategy. The model proposed in this research lies midway between the most comprehensive macroscopic formulation of heat and mass transfer, and the global formulation for which the drying medium is treated as a black box. This new model is based on a physical formulation, but should be used by people who are closely connected to the industry. To this end, the algorithm of the code named *Front_2D* is provided in the Appendix. In addition, the corresponding file can be obtained from any of the authors through the Internet.

The philosophy of the new model is to use enough physical assumptions to enable the drying equations to be resolved by a semianalytical method. This strategy allows the new model formulation to complete a two-dimensional simulation of the drying process within some seconds on a personal computer (around 5 s on a Pentium II 300 MHz, for a classic drying configuration). This efficiency in simulation time allows the model to be included in any industrial software devoted to drying.

This article is divided into different sections: model assumptions, pressure-field calculation, heat- and mass-transfer formulation, and numerical solution. The simulation results are then presented for different materials that have been dried using a variety of drying conditions. The typical anisotropic material used to validate the model is softwood. Simulating a sapwood board and a heartwood board of this species, it is shown how the model can handle different porous media and different drying conditions. Results are also depicted for light concrete. This is an isotropic material, but can be treated without any problem by *Front_2D*, and it is a good example of a porous medium with an important irreducible saturation.

Two-Dimensional Pressure Field

Keeping in mind the complexity of the coupled heat and mass transfer that occur during drying, it must be clear to the reader that the analytical model proposed in what follows is based on a set of simplifying assumptions. The real challenge is, as usual in science, to find a good compromise between how difficult it is to solve the governing set of equations on the one hand, and the variety of configurations that the new model can handle on the other. Assumptions A1 to A5 allow the two-dimensional pressure field to be resolved in terms of an analytical expression:

A1. The present model uses the basic assumption of a drying front (Hadley, 1982; Rogers and Kaviany, 1992). In 2-D, the zone where liquid evaporates to water vapor is reduced to a line. The product shape is assumed to be rectangular, with thickness l and length L. The front position is assumed to be parallel to the exchange surface. Denote e the distance between the front and the exchange surface and c the complementary distance, $c = l - e$ (Figure 1).

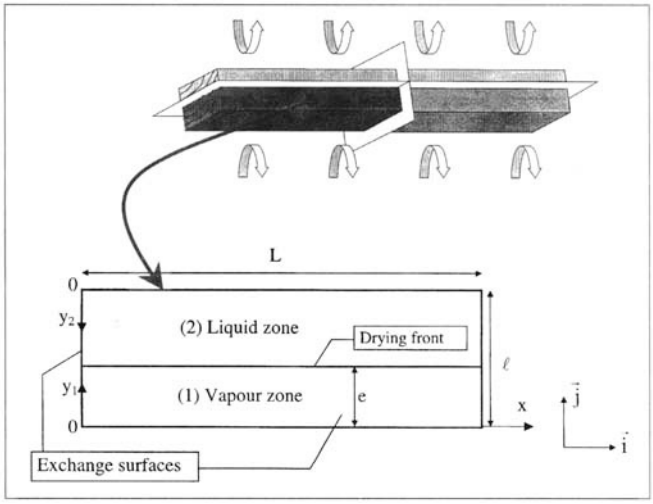

Figure 1. 2-D drying front configuration considered in this work.

A2. In the zone between the front and the exchange surface it is assumed that the gaseous phase consists only of water vapor.

A3. The water vapor is assumed to migrate only according to Darcy's law. Consequently, the diffusion term is neglected, which is consistent with assumption A2.

A4. The porous medium is divided into two zones (one vapor zone and one liquid zone). Within each zone, the physical parameters are assumed constant in space.

A5. The pressure field is assumed to have reached the steady state. Indeed, due to the ratio of liquid density over the vapor density, the front migration is always small compared to the gas velocity.

According to the assumptions (A1–A5), the pressure field throughout the sample is governed by the following sets of equations:

In the vapor zone, denoted by index 1:

$$\begin{cases} \operatorname{div}(\boldsymbol{q}_v) = 0 \\ \boldsymbol{q}_v = -\rho_v \dfrac{\overline{\overline{K}}_1}{\mu_v} \nabla P_1 \\ P_1(x=0, y_1) = P_{\text{ext}} \\ P_1(x, y_1 = 0) = P_{\text{ext}} \\ \dfrac{\partial P_1}{\partial y_1}(x, y_1 = e) = A_1 q_1(x) \quad \text{with} \quad A_1 = -\rho_v \dfrac{K_{1y}}{\mu_v} \\ \dfrac{\partial P_1}{\partial x}(x = L, y_1) = 0. \end{cases} \tag{1}$$

And in the liquid zone, denoted by index 2:

$$\begin{cases} \operatorname{div}(\boldsymbol{q}_v) = 0 \\ \boldsymbol{q}_v = -\rho_v \dfrac{\overline{\overline{K}}_2}{\mu_v} \nabla P_2 \\ \dfrac{\partial P_2}{\partial y_2}(x, y_2 = c) = A_2 q_2(x) \quad \text{with} \quad A_2 = -\rho_v \dfrac{K_{2y}}{\mu_v} \\ \dfrac{\partial P_2}{\partial x}(x = L, y_2) = 0 \\ P_2(x = 0, y_2) = P_{\text{ext}} \\ \dfrac{\partial P_2}{\partial y_2}(x, y_2 = 0) = 0. \end{cases} \tag{2}$$

Zones 1 and 2 have to be related: the pressure field and total mass flux deduced from the fluxes generated at the front position in zones 1 and 2 are continuous:

$$\begin{cases} P_1(y_1 = e) = P_2(y_2 = c) & \text{(3a)} \\ q_1(x) + q_2(x) = \langle qm \rangle. & \text{(3b)} \end{cases}$$

According to assumption (A1), the total flux that evaporates at the front level is independent of x. Nevertheless, the actual vapor flux may vary slightly along the x-axis, hence the symbol $\langle qm \rangle$, which denotes the average value along the length of the sample.

In order to focus the analytical solution on the effect of the anisotropic ratio, it is convenient to scale the system by defining

$$L^* = \frac{L}{\sqrt{\gamma}}, \quad x^* = \frac{x}{\sqrt{\gamma}}, \quad \text{and} \quad P^* = P - P_{\text{ext}}, \tag{4}$$

with

$$\gamma = \frac{K_{1x}}{K_{1y}} \neq 0.$$

The mass conservation equation in the vapor zone (Eq. 1) becomes

$$K_{1x} \frac{\partial^2 P_1^*}{\partial x^2} + K_{1y} \frac{\partial^2 P_1^*}{\partial y_1^2} = \frac{K_{1x}}{\gamma} \frac{\partial^2 P_1^*}{\partial x^{*2}} + K_{1y} \frac{\partial^2 P_1^*}{\partial y_1^2}. \tag{5}$$

Hence, because $K_{x1} \times K_{y1} \neq 0$;

$$\frac{\partial^2 P_1^*}{\partial x^{*2}} + \frac{\partial^2 P_1^*}{\partial y_1^2} = 0. \tag{6}$$

Equation 6 is the classic Laplacian equation. According to the boundary conditions, we can separate variables to seek a solution of the form:

$$P_1^*(x^*, y_1) = f(x^*) g(y_1). \tag{7}$$

Substituting this form into Eq. 8 leads to

$$f'' g + g'' f = 0$$

$$f''/f = -g''/g. \tag{8}$$

Since the lefthand side is only a function of x^* and the righthand side is only a function of y_1, the only way that the equality can hold is if both sides are equal to the same constant, say, α^2.

Hence, two separate differential equations are obtained:

$$\begin{cases} f'' - \alpha^2 f = 0 \\ g'' + \alpha^2 g = 0. \end{cases} \tag{9}$$

Taking the boundary conditions into account, α^2 must be a positive real, and the elementary solution reads:

$$P_1^*(x^*, y_1) = a \sin(\alpha x^*) \sinh(\alpha y_1). \tag{10}$$

Equation 10 satisfies the boundary conditions on the three faces of zone 1 (Eq. 1), provided that α is chosen such that

$$\left. \frac{\partial \sin(\alpha x^*)}{\partial x^*} \right|_{x^* = L^*} = 0.$$

The boundary condition on the fourth face ($y_1 = e$) can be obtained only as a weighted sum of elementary solutions:

$$P_1^*(x^*, y_1) = \sum_{k=0}^{\infty} a_k \sin(\alpha_k x^*) \sinh(\alpha_k y_1)$$

$$\text{with} \quad \alpha_k = \left(\frac{2k+1}{2L^*} \pi \right). \tag{11}$$

These elementary solutions are known to be orthogonal:

$$\int_0^{L^*} \sin(\alpha_k x^*) \sin(\alpha_q x^*) \, dx^* = \delta_{kq} \frac{L^*}{2}. \tag{12}$$

In order to determine the coefficients a_k, we have to relate zones 1 and 2 (Eqs. 1 and 2). In zone 2, the same procedure leads to the following solution:

$$P_2^*(x^*, y_2) = \sum_{k=0}^{\infty} b_k \sin(\alpha_k x^*) \cosh(\beta_k y_2). \tag{13}$$

Applying Eq. 3a leads to

$$\sum_0^{\infty} a_k \sin(\alpha_k x^*) \sinh(\alpha_k e) = \sum_0^{\infty} b_k \sin(\alpha_k x^*) \cosh(\alpha_k c). \tag{14}$$

The orthogonality property requires that

$$b_k = a_k \frac{\sinh(\alpha_k e)}{\cosh(\alpha_k c)}. \quad (15)$$

Finally, Eq. 3b allows the complete determination of the solution:

$$\sum_{k=0}^{\infty} a_k \left\{ A_1 \sin(\alpha_k x^*)\alpha_k \cosh(\alpha_k e) + A_2 \frac{\sinh(\alpha_k e)}{\cosh(\alpha_k c)} \sin(\alpha_k x^*)\alpha_k \sinh(\alpha_k c) \right\} = \langle qm \rangle. \quad (16)$$

The value of each a_k is obtained by multiplying Eq. 16 by $\sin(\alpha_k x^*)$ and integrating between 0 and L^*, using the property specified in Eq. 12; we finally obtain

$$a_k = \langle q_m \rangle \frac{2}{C\alpha_k^2 L^*}, \quad (17)$$

with $C = A_1 \cosh(\alpha_k e) + A_2 \sinh(\alpha_k e)\tanh(\alpha_k c)$.

The complete solution allows us to calculate the two-dimensional pressure field that results from a constant source $\langle q_m \rangle$ located at the front position to be determined over the entire sample. Remaining consistent with the physical assumption, this pressure field depends linearly on the flux $\langle q_m \rangle$. The most important result of this calculation is the possibility of observing and modeling very quickly the effect of the configuration: length, thickness, front position, anisotropy ratio, and the difference of permeability between the liquid and the vapor zones are all included within the expression for the solution.

As an example, Figure 2 depicts the pressure field obtained using Eqs. 11, 13, and 17 for different anisotropy ratios. The other parameters used for this calculation are $L = 25$ cm, $l = 1.5$ cm, $e = 0.5$ cm, and $\Gamma = A_2/A_1 = 0.2$ (ratio of permeability values between the liquid zone and the dry zone). It can be observed from the figure that for a small anisotropy ratio, the dimensionless pressure field is not affected by the end piece at the midlength. This is obvious for $K_x/K_y = 10$, and remains almost true for a ratio of 100. However, when the ratio γ becomes higher, one can observe how the pressure value is reduced through the sample for the same value of the vapor flux $\langle q_m \rangle$, which represents the drying rate. At this stage, we have to keep in mind that a ratio of 1,000 is a very common value for softwood species (Siau, 1984).

In fact, because of the presence of vessels within the porous structure, the anisotropy ratio can be much more important for hardwood. The last graph of Figure 2 depicts the pressure field for an anisotropy ratio of 10^4. In this case—and for the chosen values of thickness, length, and front position—almost all of the vapor transport occurs in the longitudinal direction of the sample (x-direction). The calculated streamlines and velocity fields can be the most interesting result for enabling us to understand the two-dimensional gaseous transfer (Figure 3).

Keeping in mind that the drying front moves inwards during the drying process, it is also interesting to understand

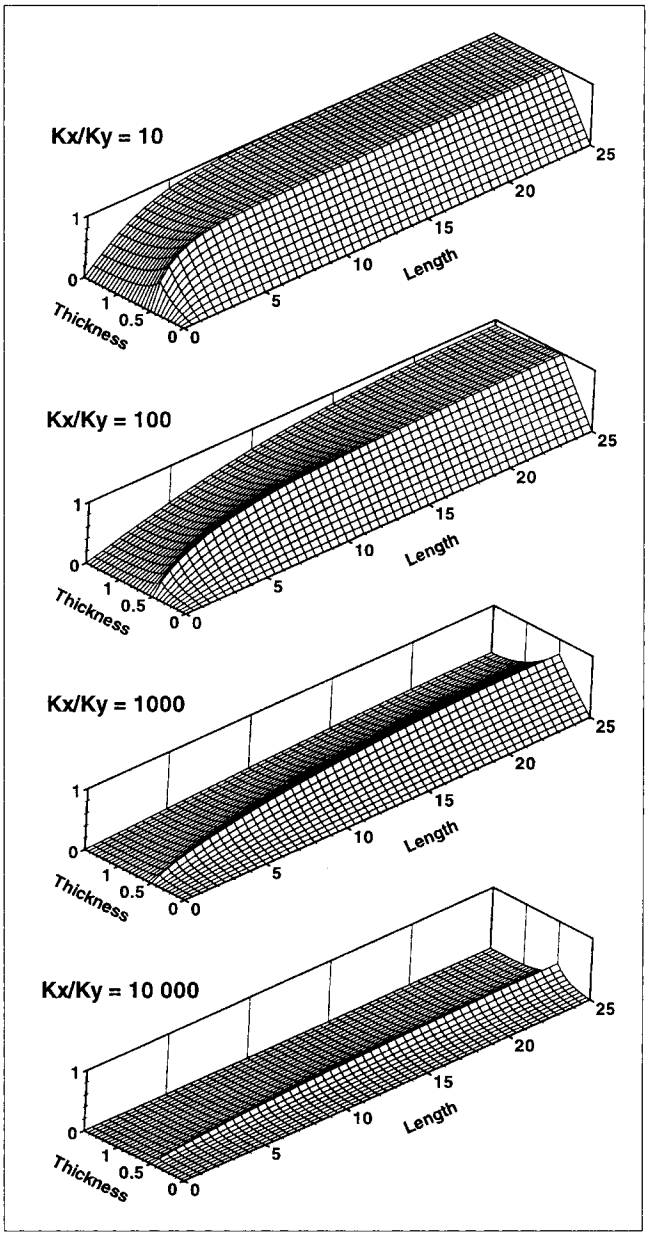

Figure 2. Analytical calculation of the pressure field for different anisotropy ratios (10, 100, 1,000, and 10^4).

how the front position and the anisotropy ratio interact. In fact, whatever the value of the anisotropy ratio, the optimal pathway for the gas migration is always along the thickness when the front is very close to the exchange surface (see Figure 4). All that must be considered is the distance required for the front position to move in order to induce a longitudinal flux. Of course, to understand the physical behavior, this distance has to be compared to the slab thickness. In the case of the parameters used in Figure 3, we can see that the permeability ratio must be larger than 100 for the longitudinal effect to become apparent for the 1.5-cm-thick slab.

The effect of length L can be explained by analyzing the solution. From Eqs. 11 and 17, we can calculate the center

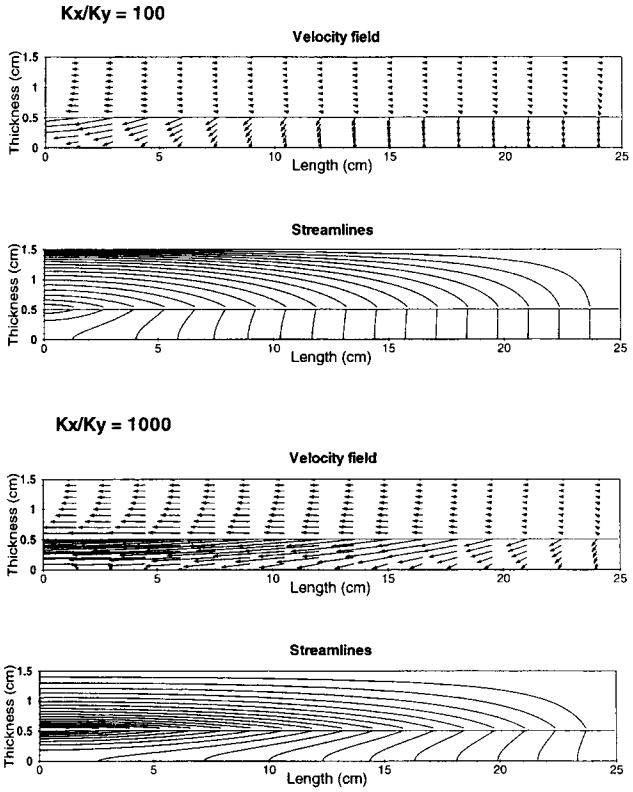

Figure 3. Velocity fields and streamlines for two different anisotropy ratios (100 and 1,000).

pressure (front position at length L^*). Rigorously, this scaled expression gives the pressure difference ΔP between the surface and this position as

$$\Delta P = \langle q_m \rangle \sum_{k=0}^{\infty} \frac{2(-1)^k}{\alpha_k^2 L^* \{A_1 \coth(\alpha_k e) + A_2 \tanh(\alpha_k c)\}}. \tag{18}$$

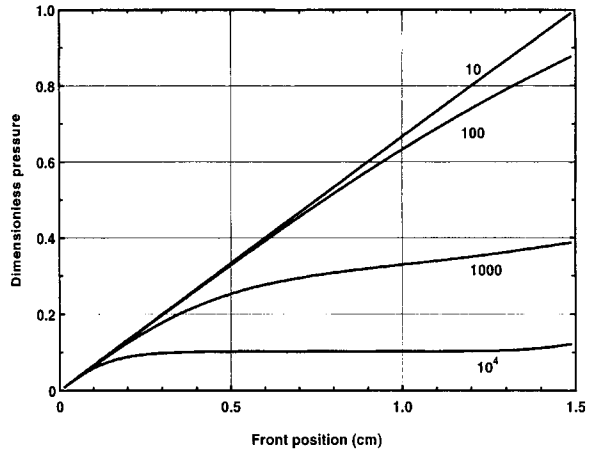

Figure 4. Effect of the permeability ratio on the front pressure at the midlength.

Rearranging Eq. 18, we obtain the following expression for the global vapor flux:

$$\langle q_m \rangle = -\rho_v \frac{K_{1y}}{\mu_v} \left(\frac{e}{\beta}\right) \frac{\Delta P}{e},$$

with

$$\beta = \sum_{k=0}^{\infty} \frac{2(-1)^k}{\alpha_k^2 L^* \{\coth(\alpha_k e) + \Gamma \tanh(\alpha_k c)\}} \tag{19}$$

and

$$L^* = \frac{L}{\sqrt{\gamma}} \qquad \alpha_k = \left(\frac{2k+1}{2L^*}\pi\right) \qquad c = l - e.$$

Equation 19 is in fact Darcy's law written in one dimension. The two-dimensional effect lies only in factor e/β. Consistently, as $e \ll L^*$, $\tanh(\alpha_k e) \approx \alpha_k e$; hence,

$$\beta \approx \frac{4e}{\pi}\left\{1 - \frac{1}{3} + \frac{1}{5} - \frac{1}{7} \cdots\right\} = e. \tag{20}$$

Hence, the factor e/β vanishes in Eq. 19. Consequently, for a porous medium that is long and not highly anisotropic, the two-dimensional model just leads to the classic Darcy's law for a slab with infinite dimension in its plane.

Conversely, as e approaches L^*, the ratio e/β becomes greater than the unit, and tends toward infinity as e/L^* increases. This expresses the increase of the mass flux, for the same value of internal overpressure, as the two-dimensional transfer takes place.

Finally, in order to know the effect of the two-dimensional gaseous migration, it is sufficient to compare the front position e with the scaled length of the board: $L^* = L/\sqrt{\gamma}$ (note that, due to the symmetry, L here is half of the real sample length). To complete the analysis, we just have to keep in mind that the ratio e/L^* varies during the process, because e varies from zero to l (for the same reason, l is half the real sample thickness).

Energy Equation

The previous calculation allowed us to determine a relation between the center overpressure and the global vapor flux. In order to define a drying model completely, it is necessary to deal with the coupling that exists between the vapor flux and the thermal flux.

Two additional assumptions allow the temperature field within the medium to be governed by a very simple linear one-dimensional differential equation.

A6. The heat transfer within the medium is assumed to occur only in the thickness of the product. Indeed, the anisotropy ratio, which can be substantial for permeability, is often much lower for thermal conductivity.

A7. The heat required to change the product temperature (sensible heat) is negligible.

Following these assumptions, the internal thermal flux is used entirely to change liquid into vapor at the front position.

According to assumption A6, the heat flux reads:

In zone 1:

$$\boldsymbol{q}_c = -\lambda_{1y}\frac{\partial T_1}{\partial y_1}\boldsymbol{j}. \tag{21}$$

In zone 2:

$$\boldsymbol{q}_c = \lambda_{2y}\frac{\partial T_1}{\partial y_2}\boldsymbol{j}. \tag{22}$$

According to assumption A7, the energy balance is governed by the following simple expressions:

In zone 1:

$$\lambda_{1y}\frac{\partial T_1}{\partial y_1}\boldsymbol{j} = -\langle q_m\rangle L_v \boldsymbol{j}. \tag{23}$$

In zone 2:

$$\lambda_{2y}\frac{\partial T_1}{\partial y_2}\boldsymbol{j} = 0. \tag{24}$$

Because the heat flux is constant within the gaseous zone, the temperature gradient is connected to the front and surface temperature values:

$$q_c = -\lambda_{1y}\frac{T_{\text{front}} - T_{\text{surf}}}{e}. \tag{25}$$

The front temperature is connected to the vapor pressure through the liquid–vapor equilibrium and sorption isotherm relationships:

$$P_{\text{front}} = P_1(x^* = L^*, y_1 = e) = P_{vs}(T_{\text{front}}) \times RH(X, T_{\text{front}}). \tag{26}$$

Finally, closure of the energy problem requires boundary conditions at the exchange surface. Here, both convective and radiative heat transfer are considered:

$$\boldsymbol{q}_{c\,\text{ext}} = h\{T_{\text{ext}} - T_1(y_1 = 0)\} + \sigma\epsilon\{T_{\text{rad}}^4 - T_1^4(y_1 = 0)\} \tag{27}$$

where h is the heat transfer coefficient, T_{ext} is the external temperature, σ the Stefan-Boltzmann constant, ϵ the equivalent emissivity factor, and T_{rad} the equivalent temperature for the radiative balance (which must account for the view factors to each of the external surfaces and their associated temperature value).

Liquid Migration

At this point, according to the configuration, the drying conditions, and the front position, we are able to relate the vapor flux to the heat flux by using the enthalpy balance. The uniqueness of the solution provides the actual drying rate through the value of the global vapor flux $\langle q_m\rangle$. Nevertheless, this value allows us to calculate the evolution in time of the averaged moisture content.

The simulation of the process requires the front position, e, to be connected to the averaged moisture content. The best situation is when the moisture-content field is known throughout the sample. Keeping the aim of this work in mind, which is to obtain a realistic but simplified model, we propose two further assumptions to describe the way in which the liquid migrates within the medium.

A8. The liquid only propagates in the thickness of the product. This means that, concerning the liquid flow, the capillary forces remain larger than the additional driving force generated by the overpressure. A one-dimensional moisture-content profile results from this hypothesis.

A9. The one-dimensional moisture-content profile has a quadratic shape. Its derivative on the plane of symmetry (at $y_1 = l$) or at the initial moisture content is equal to zero. At the exchange surface (during the first drying period), or at the front position (during the second drying period), the moisture content gradient is related to the liquid flux through the liquid migration coefficient:

$$X_l = a\xi^2 + b\xi + c, \quad \text{with} \quad \xi = y_1 - e$$

$$\boldsymbol{q}_l = -a_{ml}\nabla(X) = -\rho_l\frac{K_{y2}}{\mu_l}\frac{\partial P_c}{\partial X}\nabla(X) = \langle q_m\rangle \boldsymbol{j}. \tag{28}$$

Assumption A9 implies that $b = \langle q_m\rangle / a_{ml}$. Obviously, according to the average moisture content, the initial moisture content, the irreducible saturation, and the mass flux, several cases have to be considered (see Figure 5). Assuming that the initial moisture content, X_{ini}, is larger than the irreducible moisture content, X_{irr}, the drying always starts with case (a). Then, according to the external flux established by the drying conditions, the profile shifts toward case (b) (low liquid migration and/or high external flux) or case (c) (easy internal liquid migration and/or low external conditions). Finally, case (d) always exists, before the drying front reaches the center of the thickness. Between the drying front and the exchange surface, the moisture content is simply assumed to be linear. According to these assumptions, the computer code must be able to provide the front position in relation to the average moisture content, the drying flux, and the drying configuration (material properties, geometrical dimension, initial moisture content). This only requires some rather simple mathematical developments (the interested reader can find the resulting equations and cases in the algorithm provided in the Appendix).

Computer Code *Front_2D*

In order to simulate the drying process using the new model, a computer code has been developed using the set of equations proposed in the previous paragraphs. Due to the nonlinear expression of the external heat transfer and the effect of drying rate on the front position, an efficient nonlinear solver has been used. It consists of a Newton-Raphson

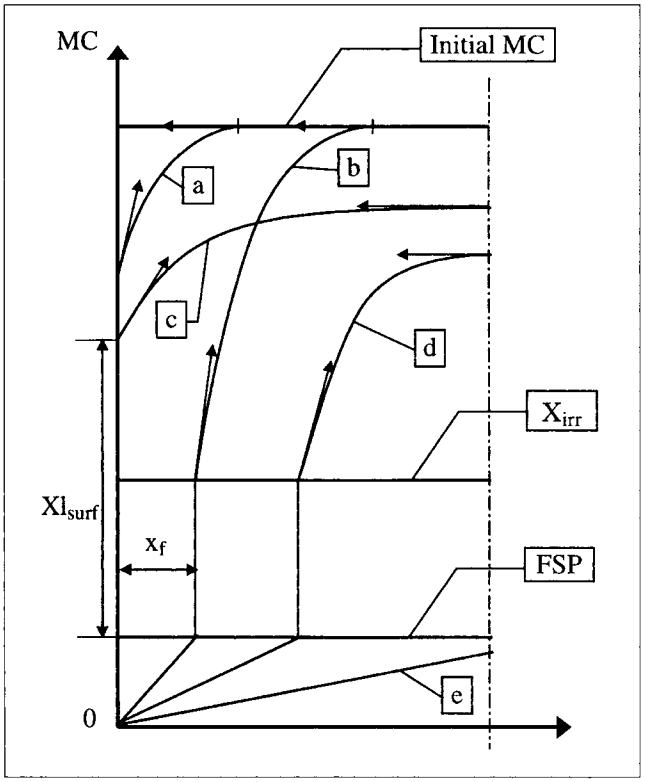

Figure 5. Moisture content profiles resulting from the assumptions concerning the liquid migration (assumptions A8 and A9).

procedure, which obtains a second-order convergence. Several sets of variables and nonlinear functions have been used. Among these tests, the best strategy was found with q_m and T_{surf} (i.e., $T_l(y_1 = 0)$ in Eq. 24) as primary variables (say u_1 and u_2) and the following nonlinear functions:

$$\mathfrak{I}_1(q_m, T_{surf}) = q_{c\,ext} - L_v \langle q_m \rangle$$
$$\mathfrak{I}_2(q_m, T_{surf}) = \langle q_m \rangle_{calc} - \langle q_m \rangle. \quad (29)$$

In the first function, the external heat flux is calculated according to Eq. 27. In the second function, the first mass flux is expressed through Eq. 19, while the second mass flux is simply the value of the primary variable.

The result is a system of nonlinear equations of the form $\mathfrak{I}(u) = 0$. The solution vector u contains the primary variables. This system must be resolved at each time step in order to advance all of the primary variables in time. It is linearized according to the complete Newton scheme. The estimate of the solution vector at the $(n+1)$th level is composed of the current solution at the nth level by writing

$$u^{(n+1)} = u^{(n)} + \delta u^{(n)} \quad (30)$$

and solving the system of linearized equations

$$J(u^{(n)})\,\delta u^{(n)} = -\mathfrak{I}(u^{(n)}) \quad (31)$$

for the correction vector $\delta u^{(n)}$. In Eq. 31, J represents the Jacobian matrix, which is computed numerically.

Finally, *Front_2D* proceeds by time increments: the drying rate is calculated for each time step, allowing the evolution of the averaged moisture content to be updated. The algorithm code is given in the Appendix. Because it does not use any programming language, this algorithm should allow any scientist to implement the structure using the programming tool of their choice.

The calculation of the Jacobian is more subtle than what is described in this synthetic structure. In fact, each time a primary variable is shifted in order to compute the derivatives, the corresponding values of the functions $\mathfrak{I}_1$ and $\mathfrak{I}_2$ have to be calculated according to the same procedure as the initial value of these functions. In particular, because the liquid moisture profile depends on the drying rate, each time the primary variable $\langle q_m \rangle$ changes, the front position e changes also, even with the same averaged moisture content. Because the gaseous phase is compressible, its density depends on the pressure. The gaseous density in Eq. 19 is calculated using the arithmetic average on the external and front pressure. This rule is exact when assuming an ideal gas for one-dimensional Darcy's law, and represents a good approximation in our two-dimensional case.

The code is written in Fortran 90 and allows a complete drying simulation in a few seconds; typically 5 seconds on a Pentium 300-MHz PC. Note that 50 terms are calculated in Eq. 19, although only a few (1 to 5) are usually required. This calculation time has to be compared with the time required when using the fastest two-dimensional version of *TransPore* (two-node approximation, structured mesh with Newton-Raphson procedure): between 5 and 10 min.

Table 1. Drying Configurations and Physical Parameters Used in Runs 1 and 2

	Run 1	Run 2	Run 3
Board	Sapwood	Heartwood	Sapwood
Half-length	25 cm	idem	idem
Half-thickness	1.5 cm	idem	idem
Temperature	**140°C**	**140°C**	**180°C**
Heat-transfer coeff. (h)	**15 W·m^{-2}·°C^{-1}**	**15 W·m^{-2}·°C^{-1}**	**50 W·m^{-2}·°C^{-1}**
Transverse permeab. (K_y)	**10^{-15} m^2**	**10^{-16} m^2**	**10^{-15} m^2**
Anisotropic ratio (K_x/K_y)	1,000	idem	idem
Thermal conduct. (λ)	0.15 W·m·°C^{-1}	idem	idem
Migration coeff. (a_{ml})	**5×10^{-6} kg·m^{-1}·s^{-1}**	**5×10^{-7} kg·m^{-1}·s^{-1}**	**5×10^{-6} kg·m^{-1}·s^{-1}**
Initial MC (X_{ini})	**150%**	**80%**	**150%**
Fiber saturation point	30%	idem	idem
Irreducible MC (X_{irr})	30%	idem	idem

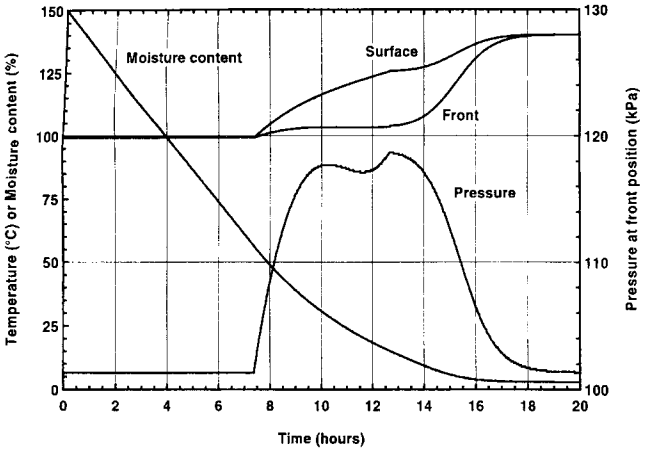

Figure 6. Semianalytical model: convective drying of sapwood at high temperature (Run 1: superheated steam, $Td = 140°C$, $h = 15$ W/m^2·°C).

MC, surface and front temperature, and front pressure vs. time.

Simulation Results

As a first overview of the possibilities offered by the present model, two simulations will be presented. Both represent convective drying of softwood with superheated steam ($T = 140°C$). The cases differ only by the part of the log: sapwood for the first run, heartwood for the second. Consistent with a previous analysis (Perré and Martin, 1994), the physical properties of these parts of the log change only for the permeability values and the initial moisture content (see Table 1).

In the case of sapwood (Run 1, Figures 6 and 7), one can observe a very long first drying period. The moisture content profiles are rather flat in the liquid domain. As a result of the assumption concerning the gaseous phase, the overpressure remains exactly equal to zero as long as the constant drying rate period lasts. For the same conditions, a simulation completed with a comprehensive set of equations would have given a slight overpressure during the first stages of the process (Perré and Turner, 1996). The physical reason for that lies in the air-part expansion and the increase in the vapor pressure when the temperature increases. Nevertheless, in the case of superheated steam, the air part can only reduce gradually, and the comprehensive simulation proves that this overpressure exists only during a short transient period.

Figures 8 and 9 depict the simulation results for the same drying conditions; however, the physical properties and initial moisture content are representative of heartwood (run 2). This test exhibits a very short first drying period, a much higher overpressure, and a total drying time that is slightly larger than the time required for sapwood, in spite of a lower initial moisture content. All of these trends are in very good agreement with the experimental observations (Salin, 1989; Perré and Martin, 1994; Perré, 1995). It is very important to note that these realistic trends, including the moisture content profiles (Pang, 1996; Rosenkilde and Arfvidsson, 1997), can be obtained regardless of the simplifying assumptions by changing parameters that are physical properties. The increase of internal overpressure is more or less directly tied to

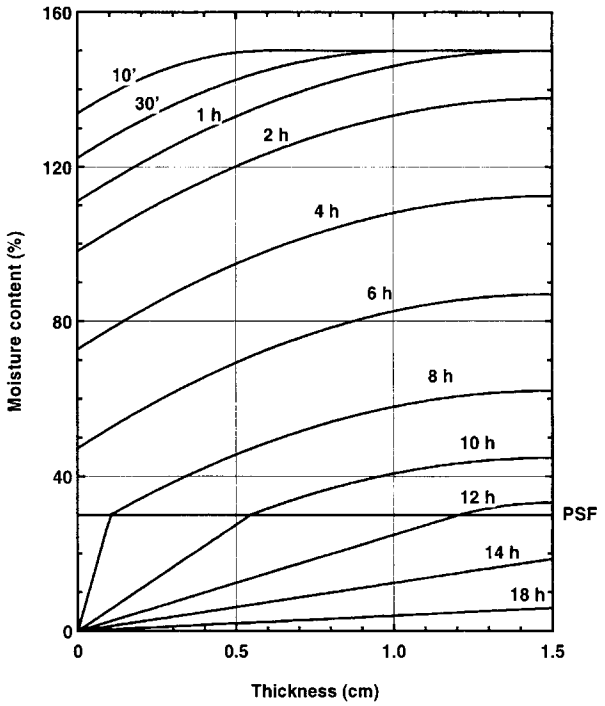

Figure 7. Semianalytical model: convective drying of sapwood at high temperature (Run 1: superheated steam, $Td = 140°C$, $h = 15$ W/m^2·°C).

Moisture content profiles at different drying times.

the value of the transverse permeability, while the duration of the constant-drying-rate period is directly connected to the liquid migration, whose gradient depends on both the drying flux and on the liquid migration coefficient.

For validation purposes, experimental results obtained for similar configurations on fir (*Abies grandis*) have been reproduced from (Perré and Martin, 1994). Figures 10 and 11 must be compared to Figures 6 and 8, respectively. The agreement

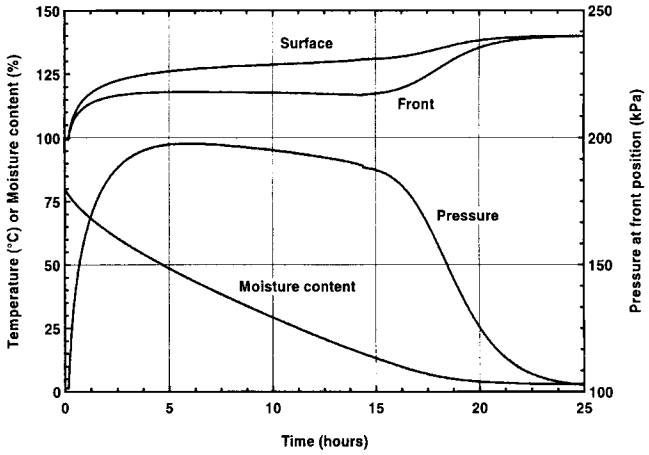

Figure 8. Semianalytical model: convective drying of heartwood at high temperature (Run 2: superheated steam, $Td = 140°C$, $h = 15$ W/m^2·°C).

MC, surface and front temperature, and front pressure vs. time.

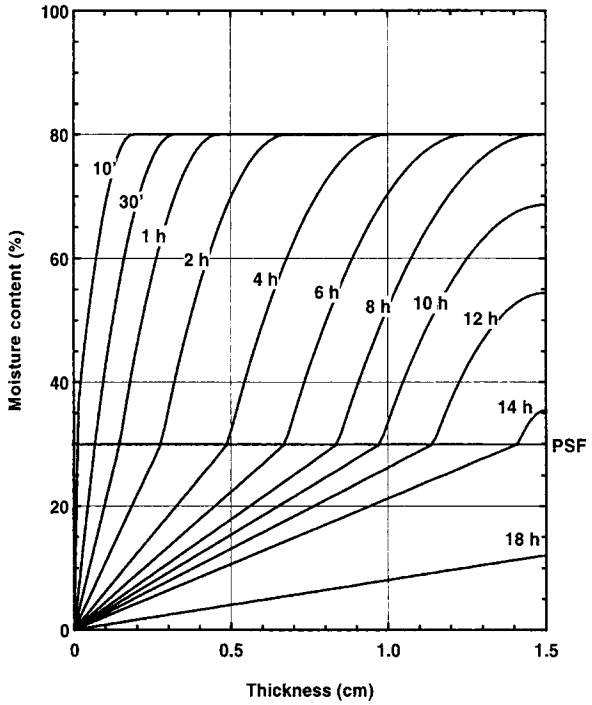

Figure 9. Semianalytical model: convective drying of heartwood at high temperature (Run 2: superheated steam, $Td = 140°C$, $h = 15$ W/m^2·°C).

Moisture content profiles at different drying times.

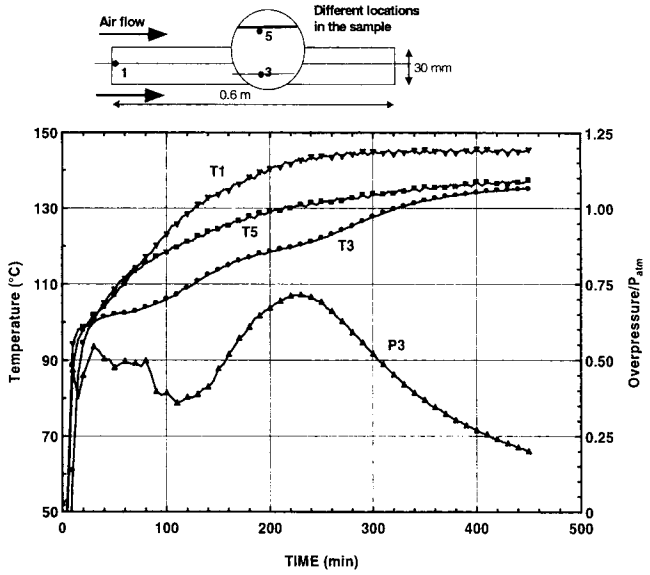

Figure 11. Experiment on heartwood: fir (*Abies grandis*) dried with superheated steam.

Temperature and internal pressure at different locations.

is rather good and proves the model is capable of producing simulations that are very fast and accurate at the same time.

In addition to the effect of material properties, the present model is also able to account for changes in the external drying conditions, and to a certain extent, to account for the coupling that exists between external conditions and internal mechanisms. A typical example is obtained for run 3, for which only the external conditions have been changed compared to run 1. This test concerns sapwood, but with severer drying conditions: higher temperature and higher heat-transfer coefficient. The constant-drying-rate period becomes very short, with a fast increase in the surface temperature from the beginning of the process (Figure 12). The calculated moisture content profiles exhibit the effect of the high external flow on the internal MC gradient. Although this is sap-

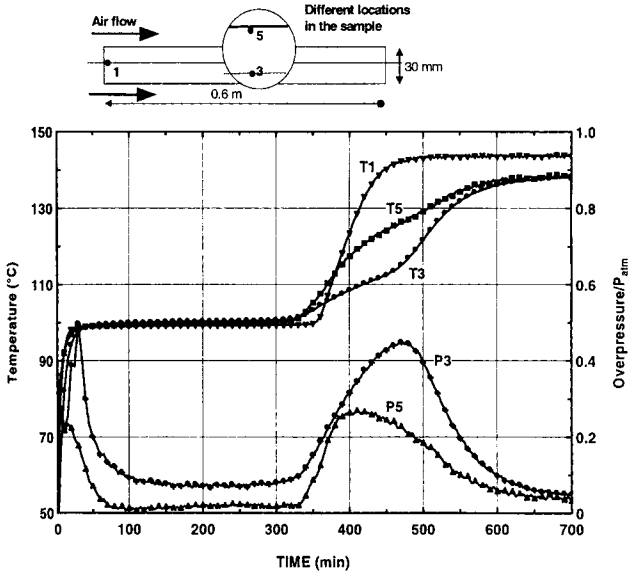

Figure 10. Experiment on sapwood: fir (*Abies grandis*) dried with superheated steam.

Temperature and internal pressure at different locations.

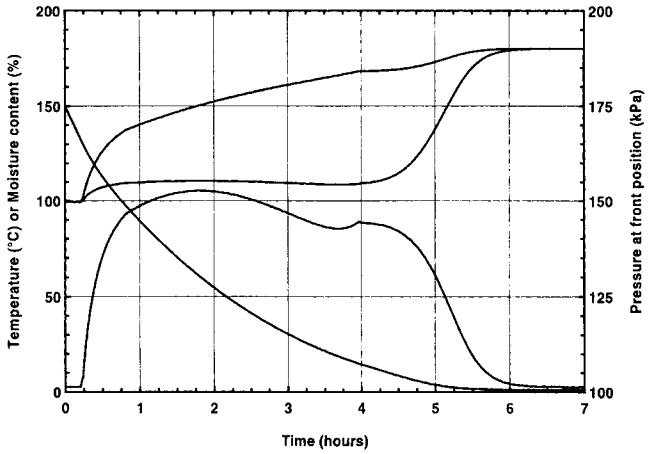

Figure 12. Semianalytical model: convective drying of sapwood at high temperature (Run 3: superheated steam, $Td = 180°C$, $h = 50$ W/m^2·°C).

MC, surface and front temperature, and front pressure vs. time.

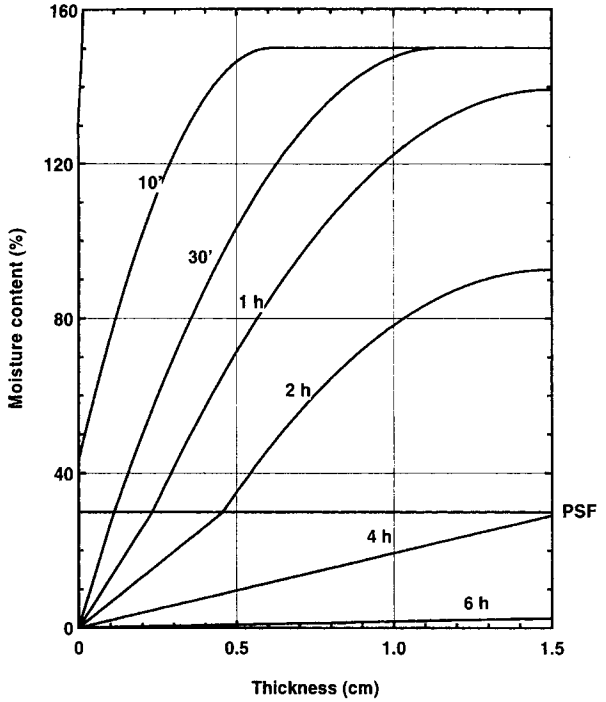

Figure 13. Semianalytical model: convective drying of sapwood at high temperature (Run 3: superheated steam, $Td = 180°C$, $h = 50$ W/m^2·°C).

Moisture content profiles at different drying times.

wood, the drying conditions are so difficult that the internal resistance to the liquid migration is higher than the external flux limitation due to the energy supplied to the slab (Figure 13). In our opinion, this result is excellent for a model that does not solve explicitly the moisture migration within the board.

The analytical solution developed to model the pressure field within the product was motivated by the high anisotropy ratios encountered for wood. This ratio consistently became one of the physical input properties of the simulation code. In order to analyze the effect of this parameter on the drying process, the anisotropy ratio has been increased, then reduced by a factor of 10, all other parameters being those of run 1 (see Table 1). Figure 14 depicts the dramatic effect of the ratio on the internal pressure: both the value and the evolution in time change when the anisotropy becomes more and more marked. For a ratio of 100, the end effect is almost negligible. Most of the mass flux must pass through the slab thickness. Consequently, the internal overpressure increases as the front position moves inward. As the longitudinal permeability becomes more and more important (1,000, then 10^4 times the transverse permeability), the internal overpressure is reduced. The evolution of the front pressure in time can even be negative. In fact, the longitudinal Darcy's flow can exist only when the gap between the drying front and the exchange surface is large enough. Then, the resistance to vapor migration is almost constant, while due to the resistance to heat transfer in the dry zone, the drying rate decreases: this means less vapor flow for the same resistance to the mass migration, hence a decrease in the front overpressure.

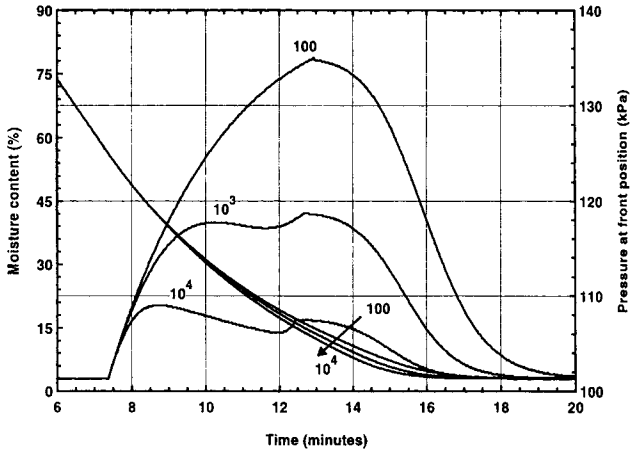

Figure 14. Semianalytical model: effect of the anisotropy ratio (sapwood, superheated steam, $Td = 140°C$, $h = 15$ W/m^2·°C).

Drying kinetics and pressure at the front position during the second drying period.

On the other hand, the evolution of the averaged moisture content seems to be affected very little by this large variation in longitudinal permeability. This observation proves that the process was mainly driven by the heat-transfer possibilities. This is consistent with the small effect the anisotropy ratio had on the evolution of the surface temperature. Indeed, the drying rate is directly proportional to the difference between the external and the surface temperatures. On the other hand, due to the change in overpressure, the front temperature is more directly affected by the possibility of longitudinal transfer. It tends to be very close to the boiling temperature of free water when resistance to mass transfer becomes negligible (Figure 15).

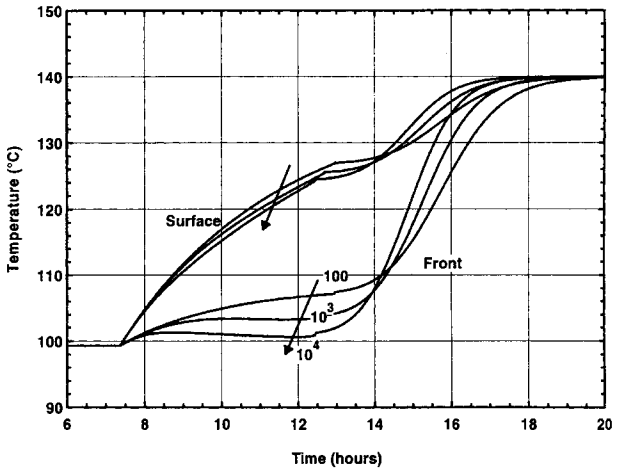

Figure 15. Semianalytical model: effect of the anisotropy ratio (sapwood, superheated steam, $Td = 140°C$, $h = 15$ W/m^2·°C).

Surface and front temperature during the second drying period.

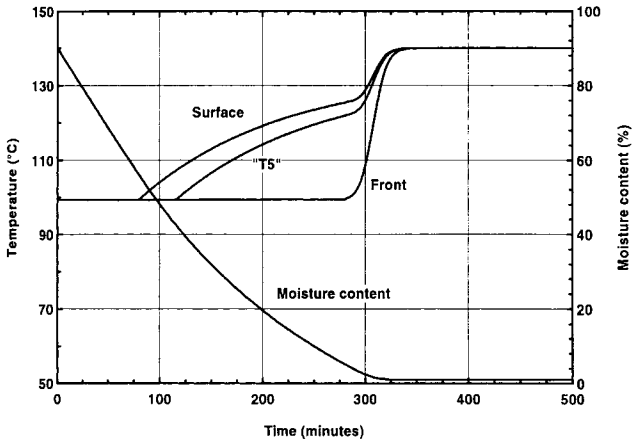

Figure 16. Semianalytical model: convective drying of light concrete at high temperature (superheated steam, $Td = 140°C$, $h = 30$ W/m^2·°C).

Temperature and internal pressure at different locations.

Finally, an example of simulation for light concrete allows other model features to be shown:

- Although developed specifically for anisotropic media, the model is also able to simulate a one-dimensional configuration of an isotropic medium (Figure 16).
- Light concrete is known to have quite high irreducible moisture content. This feature is included in the code, which calculates realistic moisture content profiles (Figure 17).
- Because this medium is well known and reproducible, all parameters used in the model can be obtained from the literature. Only the liquid migration, which here is a constant value rather than a function of the moisture content, has been adjusted according to the experiment (Figure 18, according to Perré et al., 1993). As a very good result, the obtained value is just within the variation range of the a_{ml} function in the liquid domain. This confirms that the liquid migration coefficient involved in the model is an averaged physical parameter that can be used to characterize the liquid migration within a porous medium.

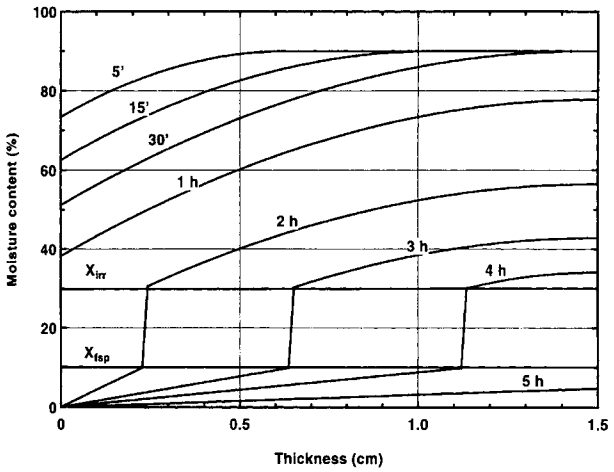

Figure 17. Semianalytical model: convective drying of light concrete at high temperature (superheated steam, $Td = 140°C$, $h = 30$ W/m^2·°C).

Moisture content profiles at different drying times.

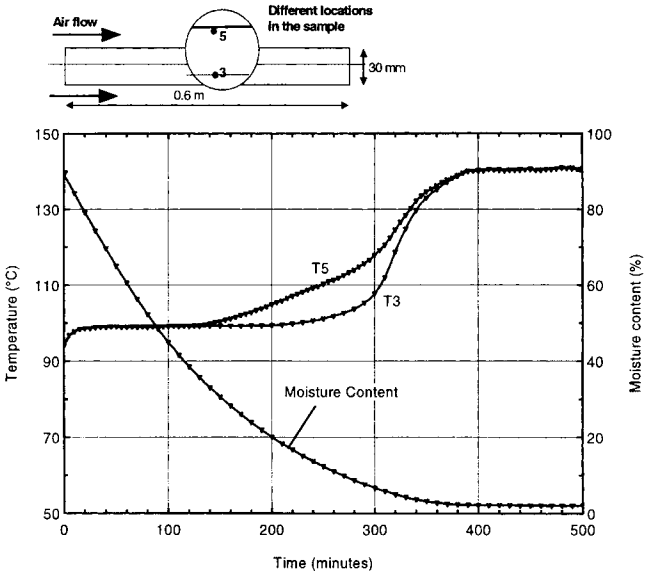

Figure 18. Experiment on light concrete dried with superheated steam.

Moisture content, surface (2 mm below the surface) and center temperature.

Conclusion

It can be seen from the extensive set of results presented throughout this research work that the developed semianalytical model provides efficient and realistic simulation results that well represent the drying process of anisotropic porous materials such as wood. Within the liquid and gaseous zones, the physical parameters are assumed constant in space. Nonetheless, the model can deal with property differences between the liquid water domain and the water vapor domain. Note that the coupling between heat and mass transfer is taken into account. This is absolutely required for describing any of the phenomena that occur during drying.

The model can be calibrated by using experimental results, with the primary fitted parameters being the averaged physical properties of the product: thermal conductivity, gaseous permeability, liquid migration coefficient, anisotropy ratio, and heat-exchange coefficient. Thereafter, the model can be used to simulate the drying process with good accuracy across a wide range of drying conditions. In fact, it is thought that the range of drying conditions that this model is capable of predicting would be much wider than for the concept of dimensionless drying curves proposed by Van Meel (1958). In particular, the drying curves calculated from the present model show how the shape of these curves depends on the material, but also depends on the drying conditions for the same material (Figure 19).

In conclusion, this model should be an excellent tool to help engineers in the design and optimization of dryers. As a consequence, and for completeness, the numerical algorithm

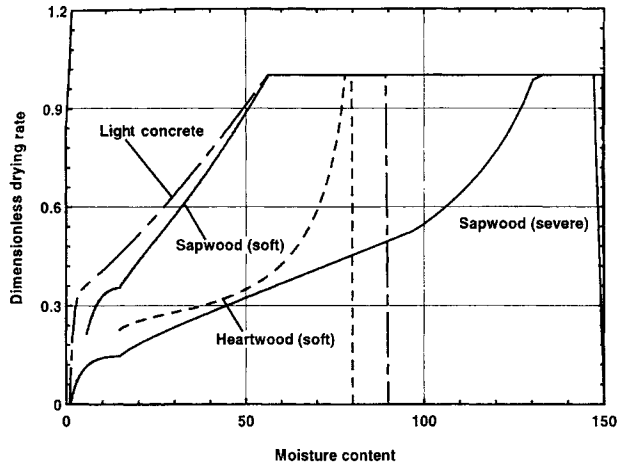

Figure 19. Dimensionless drying curves as calculated by the present model for different materials and different drying conditions.

is provided in the Appendix. As mentioned here, the code is already capable of dealing with convective and radiative heating, including vacuum drying. The next step in the advancement of this theory is to include the effects of a more advanced drying-front profile and to include the gaseous diffusion, which should extend the model possibilities to any convective and radiative drying with vapor or moist air. The dimensionless number introduced in (Perré et al., 1993) should be used for that purpose.

Notation

a_{ml} = coefficient of liquid migration, $kg \cdot m^{-1} \cdot s^{-1}$
C_p = specific heat, $J \cdot kg \cdot^{-1} \cdot K^{-1}$
$\overline{\overline{D}}$ = diffusivity, $m^2 \cdot s^{-1}$
$\mathfrak{I}_i(u_j)$ = vector function used in the Newton-Raphson procedure
L_v = latent heat of evaporation, $J \cdot kg^{-1}$
RH = relative air humidity (P_v/P_{vs})
$\overline{\overline{K}}$ = relative permeability
$\overline{\overline{k}}$ = absolute permeability, m^2
k_m = mass-transfer coefficient, $m \cdot s^{-1}$
M = molar mass, $kg \cdot mol^{-1}$
$\boldsymbol{n}$ = unit normal
P = pressure, Pa
q_c = heat-transfer flux, $W \cdot m^{-2}$
$\boldsymbol{r}$ = residual vector
R = gas constant, $J \cdot mol^{-1} \cdot K^{-1}$
t = time, s
$\boldsymbol{v}$ = velocity, $m \cdot s^{-1}$
X_{FSP} = fiber saturation point
x = longitudinal direction
y = transverse direction
α = interpolation factor
γ = anisotropy ratio for permeability (K_x/K_y)
Γ = permeability ratio between dry and moist zones (K_{y1}/K_{y2})
ϕ = porosity, $m^3 \cdot m^{-3}$
μ = dynamic viscosity, $kg \cdot m^{-1} \cdot s^{-1}$
ρ = density, $kg \cdot m^{-3}$

Superscripts and subscripts

cr = critical
eff = effective property
eq = equilibrium
g = gas phase
i = general index for vectors
sat = saturated
v = vapor

Literature Cited

Hadley, G. H., "Theoretical Treatment of Evaporation Front Drying," *Int. J. Heat Mass Trans.*, **25**, 1511 (1982).

Marinos-Kouris, D., Z. B. Maroulis, and C. T. Kiranoudis, "Computer Simulation of Industrial Dryers," *Drying Technol. J.*, **14**, 971 (1996).

Pakowski, Z., and R. Zylla, "Construction of Integrated Software for Drying Calculations," *Drying Technol. J.*, **14**, 463 (1996).

Pang, S., "Moisture Content Gradient in a Softwood Board During Drying: Simulation from a 2-D Model and Measurement," *Wood Sci. Technol.*, **30**, 165 (1996).

Perré, P., "Drying with Internal Vaporization: Introducing the Concept of Identity Drying Card," *Drying Technol. J.*, **13**, 1077 (1995).

Perré, P., M. Moser, and M. Martin, "Advances in Transport Phenomena during Convective Drying with Superheated Steam or Moist Air," *Int. J. Heat Mass Trans.*, **36**, 2725 (1993).

Perré, P., and M. Martin, "Drying at High Temperature of Heartwood and Sapwood: Theory, Experiment and Practical Consequence on Kiln Control," *Drying Technol. J.*, **12**, 1915 (1994).

Perré, P., and I. W. Turner, "Using a Set of Macroscopic Equations to Simulate Heat and Mass Transfer in Porous Media: Some Possibilities Illustrated by a Wide Range of Configurations that Emphasize the Role of Internal Pressure," *Numerical Methods and Mathematical Modelling of the Drying Process*, I. W. Turner and A. Mujumdar, eds., Marcel Dekker, New York, p. 83 (1996).

Salin, J. G., "Remarks on the Influence of Heartwood Content in Pine Boards on Final Moisture Content and Degrade," *Proc. IUFRO Wood Drying Symp.*, Seattle, WA, p. 4 (1989).

Turner, I. W., and P. Perré, "A Comparison of the Drying Simulation Codes *TRANSPORE* and *WOOD2D* which are Used for the Modelling of Two-Dimensional Drying Processes," *J. Drying Technol. Spec. Ed. Math. Modelling Numer. Simulation*, **3**, 695 (1995).

Rosenkilde, A., and J. Arfvidsson, "Measurements and Evaluation of Moisture Transport Coefficients during Drying of Wood," *Holzforchung*, **51**, 372 (1997).

Rogers, J. A., and M. Kaviany, "Funicular and Evaporating-Front Regimes in Convective Drying of Granular Beds," *Int. J. Heat Mass Trans.*, **35**, 469 (1992).

Siau, J. F., *Transport Processes in Wood*, Springer-Verlag, New York (1984).

Van Meel, D. A., "Adiabatic Convection Batch Drying with Recirculation of Air," *Chem. Eng. Sci.*, **9**, 36 (1958).

Appendix

Program Front_2D

Set thermophysical constants
Set geometrical parameters
Set initial conditions
Set external conditions
Set internal transfer parameters
Set computation parameters, including time step *dt*

Open saving files (profiles and kinetics)
Loop until final drying time
Compute front position e
If $(e = 0)$ **Then** (constant drying rate period)
Set $T_{surf} = T_{boiling}$
Set $T_{front} = T_{boiling}$
Compute $\langle q_m \rangle = \dfrac{q_{c\,ext}}{L_v}$ according to Eq. 27
Else (falling drying-rate period)
Choose $T_{surf}^{(0)}$ and $\langle q_m \rangle^{(0)}$
Set $i = 0$
Loop until stopping criterion has been satisfied
Compute front position e
Compute $q_{c\,ext}$
Compute $T_{front} = T_{surf} - \dfrac{\langle q_m \rangle^{(i)} \times L_v}{\lambda \times e}$, hence $P_{v\,front}$
Compute $\langle q_m \rangle_{calc}$ according to Eq. 19
Compute $\Im_1$ and $\Im_2$
Compute Jacobian J (by shifting each primary variable and computing $d\Im_1$ and $d\Im_2$)
Compute du
Set $T_{surf}^{(i+1)} = T_{surf}^{(i)} + du_1$
Set $\langle q_m \rangle^{(i+1)} = \langle q_m \rangle^{(i)} + du_2$
Set $i = i + di$
End Loop
End If
Compute $d\langle X \rangle = \dfrac{\langle q_m \rangle \times dt}{\rho_s \times l}$
Set $\langle X \rangle (t + dt) = \langle X \rangle (t) + d\langle X \rangle$
Set $t = t + dt$
If (save data required) write values in saving files
End Loop
End program Front_2D

Subroutine liquid_migration (Input: $\langle q_m \rangle$, $\langle X \rangle$, X_{ini}, X_{irr}, X_{FSP}, and l; **Output:** e and RH)
Set $X_{l\,ini} = X_{ini} - X_{irr}$
Set $b = \dfrac{\langle q_m \rangle}{a_{ml}}$ and $a = -\dfrac{b^2}{4X_{l\,ini}}$
Set $x_{cr} = \dfrac{2X_{l\,ini}}{b}$
If $(x_{cr} \le l)$ **Then** (*sequence a, b, d and e in Figure 5*)
Set $X_1 = \dfrac{a x_{cr}^3}{3} + \dfrac{b x_{cr}^2}{2}$
Set $X_{cr} = X_{irr} + \dfrac{X_1 + X_{l\,ini} \times (l - x_{cr})}{l}$
If $(\langle X \rangle \ge X_{cr})$ **Then** (*case a*)
Set $e = 0$
Set $RH = 1$
Else
Set $X_2 = \dfrac{X_1 + X_{irr} \cdot x_{cr} + 0.5 X_{FSP}(l - x_{cr})}{l}$
If $(\langle X \rangle) \ge X_2)$ **Then** (*case b*)
Set $e = -\dfrac{l \times (\langle X \rangle - X_{ini}) - (X_1 + X_{l\,ini} x_{cr})}{X_{ini} - 0.5 X_{FSP}}$
Set $RH = 1$
Else If $(\langle X \rangle \ge 0.5 X_{FSP})$ **Then** (*case d*)
Solve $Ae^2 + Be + C = 0$ with $\begin{cases} A = b/3 \\ B = -2Al + 0.5X_{FSP} - X_{irr} \\ C = l \times (Al + X_{irr} - \langle X \rangle) \end{cases}$

Set $RH = 1$

Else (*case e*)

Set $e = l$

Set $RH = 1 - \exp[-x^*(0.76469 + 3.67872x^*)]$ with $x^* = \dfrac{2\langle X \rangle}{X_{FSP}}$

End If

End If

Else (*sequence a, c, d and e in Figure* 5)

Set $X_{cr} = \dfrac{bl}{3} + X_{irr}$

If $(\langle X \rangle \geq X_{cr})$ **Then** (*case a or c*)

Set $e = 0$

Set $RH = 1$

Else If $(\langle X \rangle \geq = 0.5X_{FSP})$ **Then** (*case d*)

cf. above

Else (*case e*)

cf. above

End If

End If

Manuscript received June 16, 1998, and revision received Oct. 13, 1998.